Backward multiplex coherent anti-Stokes Raman (CARS) spectroscopic imaging with electron-multiplying CCD (EM-CCD) camera

Murakami, Yusuke; Yoshimura, Minami; Klement, W. J. Niels; Oda, Atsuki; Sakamoto, Ryo; Yakabe, Miho; Matsumoto, Atsushi; Oketani, Ryosuke; Leproux, Philippe; Ikenouchi, Junichi

Published in:
OSA Continuum

DOI:
10.1364/OPTCON.497869

Publication date:
2023

Research Article Vol. 2, No. 9 / 15 Sep 2023 / Optics Continuum 2044
OPTICS CONTINUUM

Backward multiplex coherent anti-Stokes Raman (CARS) spectroscopic imaging with electron-multiplying CCD (EM-CCD) camera

YUSUKE MURAKAMI,[1,2] MINAMI YOSHIMURA,[3] W. J. NIELS KLEMENT,[4] ATSUKI ODA,[3] RYO SAKAMOTO,[3] MIHO YAKABE,[3] ATSUSHI MATSUMOTO,[5] RYOSUKE OKETANI,[3] PHILIPPE LEPROUX,[6] JUNICHI IKENOUCHI,[5] WESLEY R. BROWNE,[4] AND HIDEAKI KANO[3,*]

[1]*Ph.D. Program in Humanics, University of Tsukuba, 1-1-1 Tennodai, Tsukuba, Ibaraki 305-8577, Japan*
[2]*International Institute for Integrative Sleep Medicine (WPI-IIIS), 1-1-1 Tennodai, Tsukuba, Ibaraki 305-8575, Japan*
[3]*Department of Chemistry, Faculty of Science, Kyushu University, 744, Motooka, Nishi-ku, Fukuoka 819-0395, Japan*
[4]*Molecular Inorganic Chemistry, Stratingh Institute for Chemistry, Faculty of Science and Engineering, University of Groningen, Nijenborgh 4, 9747AG Groningen, The Netherlands*
[5]*Department of Biology, Faculty of Sciences, Kyushu University 774 Motooka, Nishi-ku, Fukuoka 819-0395, Japan*
[6]*Institut de Recherche XLIM, UMR CNRS No. 7252, 123 Avenue Albert Thomas, 87060 Limoges CEDEX, France*
[*]*hkano@chem.kyushu-univ.jp*

Abstract: A multiplex CARS imaging system, equipped with an EM-CCD camera, was developed to improve the sensitivity of backward CARS imaging in biological analysis using an inverted microscope. The signal-to-noise ratio was improved by a factor of ca. 3 compared to a conventional CCD mode through the use of EM gain. When imaging epithelial cells in the backward CARS configuration, intracellular organelles such as lipid droplets and nuclei were spectroscopically identified with an exposure time of only 100 ms/pixel.

1. Introduction

Raman microscopy is a powerful method for chemically selective, non-invasive, label-free single-cell-analytical imaging for investigating living cells without cell disruption [1–9]. Thanks to the molecule specific vibrational contrast, various kinds of intracellular metabolites have been visualized in a label-free manner [10–20]. Since ordinary Raman scattering is a weak process, coherent Raman scattering such as coherent anti-Stokes Raman scattering (CARS) [10–12] and stimulated Raman scattering (SRS) [13–15,19,21] processes have been widely employed to boost the weak Raman signal, and obtain Raman images with high sensitivity and high speed. Recently, coherent Raman microscopy has been extended to a spectroscopic imaging technique [7,6]. In particular, ultra-broadband multiplex CARS spectroscopic imaging [22–25] enables us to obtain both CARS images and spectra with a spectral coverage of approximately 3000 cm^{-1}, spanning the entire region of the fundamental vibrational modes [22,26–29]. CARS spectroscopic imaging has been applied to a study on liquid-liquid phase separation *in vitro* [30] and *in-vivo* visualization of algae [31,32] and bacteria [25,33], liver diagnosis [34], enzymatic reaction [35], and spatially resolved omics [36], revealing intracellular accumulation of a wide variety of metabolites. Moreover, new techniques have been reported using CARS spectroscopic imaging

#497869 https://doi.org/10.1364/OPTCON.497869
Journal © 2023 Received 13 Jun 2023; revised 20 Jul 2023; accepted 4 Sep 2023; published 8 Sep 2023

OPTICS CONTINUUM

such as super-resolved imaging [37], surface-enhanced imaging [38], and Fourier-transformation CARS imaging [39].

Regarding the application of CARS microscopy in life sciences, the forward scattering properties of CARS can pose a practical problem. To detect the strong forward CARS signal enhanced with the phase matching condition [40], another objective lens is typically used on the opposite side of the illumination objective lens [3–5]. However, in the inverted microscope commonly used in the life science field, only one objective lens is used for both illumination and detection. This configuration makes it difficult to install a forward CARS detection system.

One solution to this problem is to use weak backward CARS detection. Several studies have reported the detection of backward CARS using an inverted microscope or a fiber endoscope with a pulsed laser source [2,41–43]. This backward CARS signal is primarily due to a diffused forward CARS signal from opaque samples such as tissue (see Fig. 1), which produces a relatively strong backscattered forward CARS signal. However, in thin, transparent samples such as cells, the diffused forward CARS signal is negligible and only a weak, phase-mismatched backward CARS signal appears [40,44,45]. To date, there have been no report on backward CARS *spectra* under a microscope, except for the results obtained from measuring the diffused forward CARS spectra [41]. Therefore, signal amplification techniques are needed to perform spectroscopic imaging of the backward CARS signal at a rate comparable to that of forward CARS.

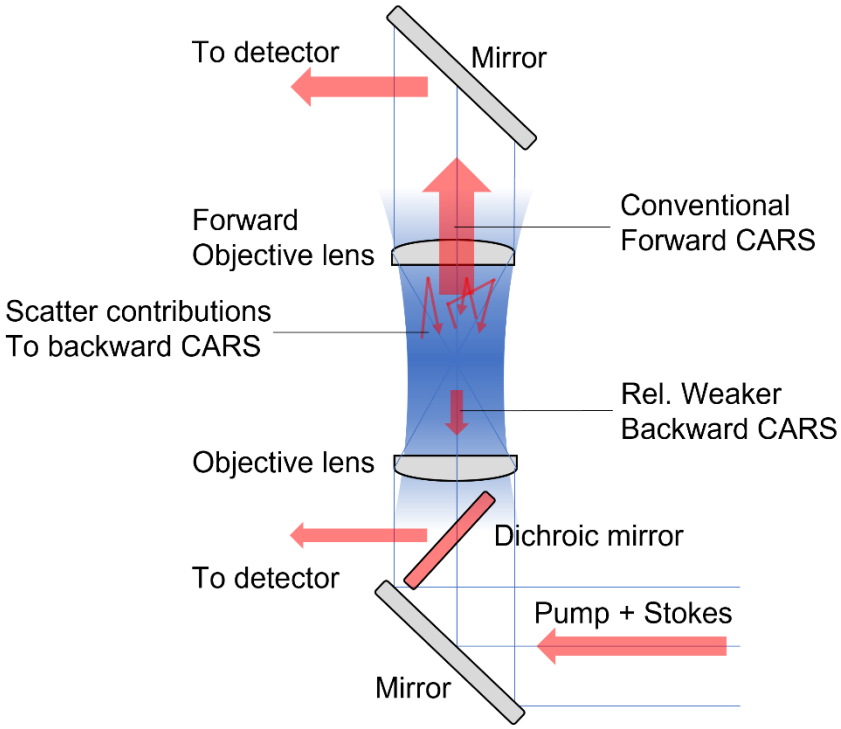

Fig. 1. Illustration of the CARS signal generation. Concerning the backward configuration, the scattering of the forward CARS signal is dominant for opaque samples. On the other hand, for transparent or thin samples such as cells, the inherent and weak backward CARS signal is mainly detected.

Here we used an electron-multiplying charge coupled device (EM-CCD) camera to improve the detection efficiency and signal-to-noise ratio (SNR) of the backward CARS signal. Although EM-CCD cameras have been employed for spontaneous Raman microscopy [16,18,20,46,47],

OPTICS CONTINUUM

the application to coherent Raman microspectroscopy has still been limited [48]. This is because most studies on coherent Raman microspectroscopy, including ours [28,29], focus on the forward CARS detection, for which a conventional CCD camera is sufficient [33]. First, we describe the experimental setup with an EM-CCD camera. We then evaluated the SNR and impact of EM gain. Finally, we demonstrated CARS imaging of epithelial cells.

2. Methods

2.1. Backward multiplex CARS spectroscopic imaging system

The backward multiplex CARS signal was collected by a home-made nonlinear optical microscope equipped with a custom-made, dual-fiber output synchronized light source (OPERA HP, Leukos, Limoges, France) [33], which was modified for the backward signal collection as shown in Fig. 2. The first laser output had a wavelength of 1064 nm, a pulse width of 50 ps, and a repetition rate of 1 MHz, and was used as the pump beam (ω_1) for the CARS process. The second laser output was passed through a photonic crystal fiber (PCF) to provide supercontinuum (SC) radiation ranging from visible to near infrared (NIR) with a broad spectral range of 1100-1800nm, which was used as the Stokes beam (ω_2). The pump and Stokes laser beams were superimposed by an edge filter (LP02-1064RE-25, Semrock, Rochester, NY) and were guided into a modified inverted microscope (ECLIPSE Ti, Nikon Corporation, Tokyo, Japan). Two laser beams were tightly focused on the sample through an objective (CFI Plan Apo 60x NA 1.27, water-immersion, Nikon Corporation). The sample was placed on a piezoelectric stage (Nano-LP200, Mad City Labs, Madison, WI) for position selection. The full scanning range of the xyz-piezo stage was 200 μm^3. The backscattered CARS signal ($2\omega_1$ - ω_2) was spectrally separated by a dichroic mirror (Di02-R980-25 × 36, Semrock, NY), and was detected using a spectrometer (Kymera 193i, Andor Technology, Belfast, UK) equipped with an EM-CCD camera (Newton DU 970P, Andor Technology, Belfast, UK) to enhance the weak CARS signal. The groove and blaze wavelength of the grating in the spectrometer were 300 G/mm and 1200 nm, respectively. The spectral coverage and spectral resolution of the CARS signal were ~3500 cm^{-1} and 14 cm^{-1}, respectively. The forward CARS signal can also be collected using the second objective (Plan S Fluor 40× NA 0.6, Nikon Corporation), and detected using the same spectrometer and the EM-CCD camera just by switching the flip-mounted mirror indicated by A in Fig. 2.

2.2. Sample preparation

We utilized polystyrene beads (Polysciences Inc.) with a diameter of 10 μm to evaluate the performance of the present system. The original aqueous suspension of the beads was diluted more than 10 times, and approximately 5 μl of the suspension was sandwiched between a cover glass and a glass slide, then sealed with nail polish.

EpH4 cells derived from a mouse mammary epithelial cell were used as cultured cell samples. Cells were cultured on coverslips soaked in Dulbecco's Modified Eagle's Medium supplemented with 10% fetal bovine serum and incubated in a humidified incubator containing 5% CO_2 in air at 37 °C for 3 days. The coverslip was removed from the medium immediately before measurement. The cells on the cover glass were flipped over, sandwiched with a glass slide, and sealed with nail polish. An on-stage incubator was useful in particular for time-lapse CARS study [49], however in the present study an incubator was not necessary due to the short overall measurement time.

OPTICS CONTINUUM

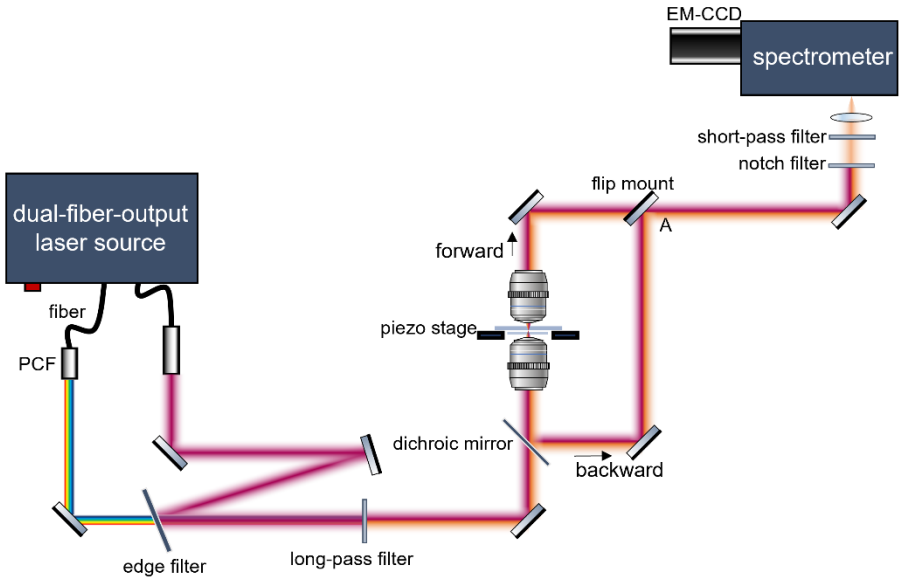

Fig. 2. Experimental setup of a backward multiplex CARS spectroscopic imaging system with an EM-CCD camera. The conventional forward CARS signal can also be obtained using the same detector by flipping the mirror mount indicated by A.

3. Results and discussion

3.1. Evaluation of EM-gain dependence of the backward CARS signal

The performance of the system with an EM-CCD camera was evaluated using the backward CARS signals of polystyrene beads with a diameter of 10 µm. Figure 3(a) shows CARS spectra with the EM-gain value of 200 and of 255 (maximum). For reference, the CARS signal with the conventional mode is also shown. We used photo-generated electrons as a vertical axis rather than the CCD counts to compare the EM mode with the conventional mode, because the conversion ratio of photo-generated electrons to CCD counts was different between the EM mode (4.3 count/electron) and the conventional CCD mode (1.3 count/electron). The CARS spectra with the EM gain 255 and 200 indicate that the signal intensity is not proportional to the value of the EM gain, and the signal is amplified enough to be visible in comparison with the conventional CCD. We also evaluated the issue of etaloning on the back-illuminated CCD, which gives fringing in the spectral profile in the NIR region. The 1064-nm pump generates the CARS signal in the range of 746-1010 nm. To suppress the effect of etaloning in this range, back-illuminated, deep-depletion CCD cameras are often used in measurements [28,29]. However, deep-depletion type EM-CCD cameras are not currently available. Since the EM-CCD camera used in this study consists of the normal back-illuminated CCD, the etaloning may be visible in the spectral range in the present study. Due to the relative intensity of the noise in the CARS spectrum (Fig. 3(a)), however, the impact of fringing is not prominent in the backscattered CARS signal. On the other hand, it is noticeable in the forward CARS signal in the fingerprint region shown in Supplement 1, Fig. S1.

Next, we will focus on the nonlinear dependence of the CARS signal on the EM-gain value. Figure 3(b) depicts the EM-gain dependence of the backward CARS signal at 1003 cm^{-1}. As shown in Fig. 3(a), the signal exhibits a sharp vibrational resonance attributed to the phenyl-ring breathing mode. The vertical axis in Fig. 3(b) is indicated as enhancement factor, which is calculated by dividing the CARS signal intensity at each EM-gain value with that at the

OPTICS CONTINUUM

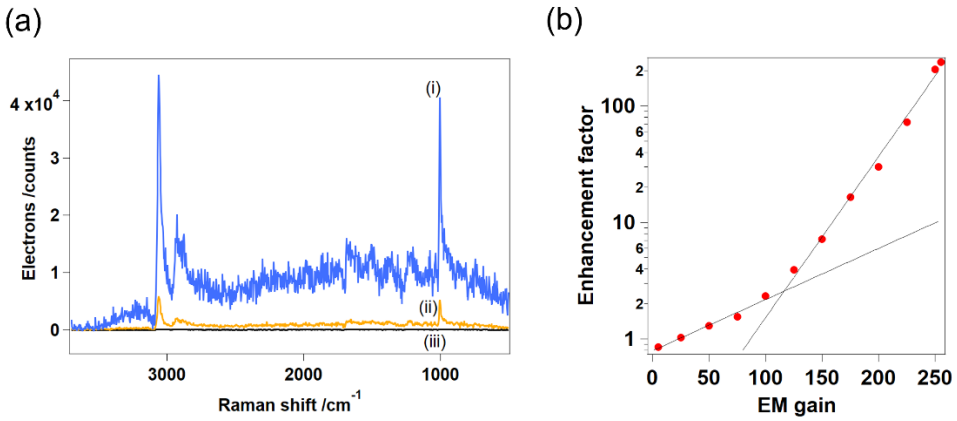

Fig. 3. Backward CARS signal detected by an EM-CCD camera. (a) Spectral profiles of the raw CARS signal of a polystyrene bead with the EM-gain value of (i) 255, (ii) 200, and (iii) conventional mode. (b) EM-gain dependence of the photo-generated electrons corresponding to the CARS signal intensity (red). The CARS signal at 1003 cm^{-1} is evaluated. The vertical axis is indicated as enhancement factor, which is calculated by dividing the CARS signal intensity at each EM-gain value with that at the conventional mode. The exposure time was 50 ms on the software, corresponding to 18 fps. The solid lines represent the results fitted with an exponential function for the eye guide phenomenologically. It is proportional to exp(0.01x) for $x < 100$, while exp(0.03x) for $x > 150$, respectively. Here x represents the EM-gain value.

conventional mode. The laser power for ω_1 and ω_2 was fixed to approximately 45 mW and 170 mW, respectively. The exposure time at each pixel was 50 ms, corresponding to 18 frame-per-second (fps) due to finite readout time. As pointed out in Fig. 3(a), the CARS signal intensity is amplified nonlinearly with respect to the EM gain. It initially increased roughly with exp(0.01x) against the EM-gain value x ($x < 100$), then increased with exp(0.03x) when $x > 150$. In both cases, the signal intensity was found to increase exponentially against the EM-gain value. Figure 4 summarizes the results of backward CARS imaging of polystyrene beads. Figure 4(a) indicates a bright field image. Figure 4(b) shows the comparison between the conventional mode and the EM-gain mode with the value of 255. The spectral profiles indicated by (i) and (ii) in Fig. 4(b) correspond to the raw CARS signals at the red crosses in Fig. 4(c) and (d), respectively. The aromatic CH stretching (3060 cm^{-1}) and phenyl-ring breathing (1003 cm^{-1}) vibrational modes were observed at the gray hatched regions for the EM mode (i), while these resonances were hardly observed for the conventional mode. Figure 4(c) and (d) show backward CARS images at 1003 cm^{-1} for the conventional and EM modes, respectively. The exposure time per pixel was 0.57 ms (on the software). Due to the finite readout time, the frame rate was 440 fps. The line profiles below the images shown in Fig. 4(e) and (f) correspond to the dotted horizontal line in Fig. 4(c) and (d). Comparing the two images, the CARS image in the EM mode gives a much clearer contrast than that in the conventional mode. The EM mode gives distinct signal intensity at the position of a bead. Therefore, it was demonstrated that the EM mode is better than the conventional mode.

In order to evaluate the improvement quantitatively, we compared SNR in the EM mode with that in the conventional mode. To calculate SNR, white and black areas indicated in the inset of Fig. 4(d) were used as the noise and the signal regions. The SNR is calculated using the following equation,

$$SNR_{\mathrm{RMS}} = \frac{I_{\mathrm{av}} - N_{\mathrm{av}}}{N_{\mathrm{RMS}}},$$

OPTICS CONTINUUM

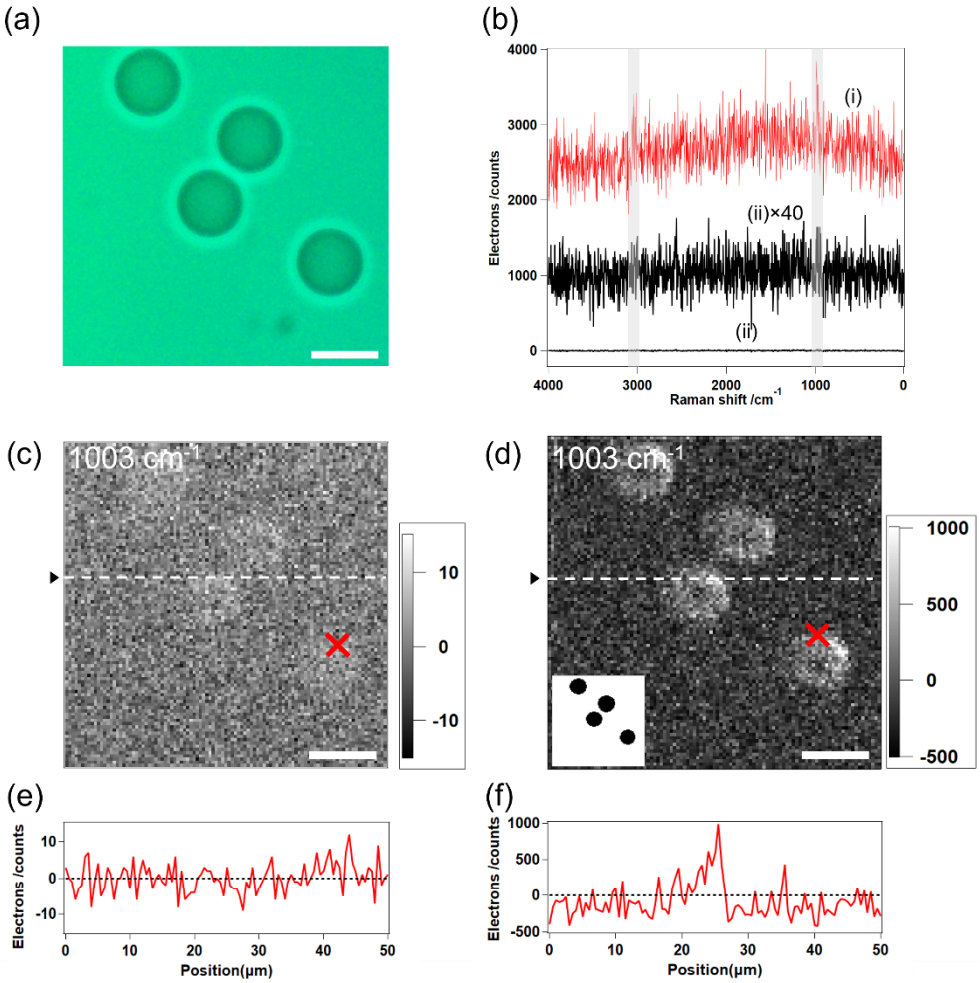

Fig. 4. Backward CARS imaging of polystyrene beads with an EM-CCD camera. (a) Bright field image. (b) Spectral profiles of the raw backward CARS signal indicated by (i) and (ii), corresponding to the red crosses at (c) and (d). (c and d) Backward CARS images at 1003 cm^{-1} by the conventional mode (c) and EM-gain mode at the value of 255 (d). (e and f) Line profiles of the broken lines in (c) and (d). Inset in (d): binary image converted from (d). The white and black areas correspond to the signal and noise areas, respectively. The white areas were defined as noise and black areas as signal to calculate SNR. The image size (pixels and microns) and step size were 101×101, 50×50 μm^2, and 0.5 μm, respectively. The scale bar is 10 μm. The exposure time was 0.57 ms on the software. Due to the finite readout time, the frame rate was 440 fps.

OPTICS CONTINUUM

where

$$N_{\mathrm{RMS}} = \sqrt{\frac{\sum_{i=1}^{n} (N_{\mathrm{i}} - N_{\mathrm{av}})}{n}}.$$

Here SNR_{RMS} is the SNR calculated by the RMS method. I_{av} is average value of the CARS signal at the signal region indicated in Fig, 4(d), N_{av} is average value of the noise at the noise region in Fig. 4(d), N_{RMS} is the RMS, N_{i}, is the noise at i-th spatial pixel, n is the total number of the pixels at the noise region. The values of the SNR were calculated to be 0.73 and 1.98 for the conventional and the EM-gain mode at the value of 255, respectively. Based on these results, the SNR was improved by a factor of ca. 3 for the EM mode, indicating the usefulness of an EM-CCD camera in the backward configuration.

Finally, we will focus on the unique image formation using the backward CARS signal. The backward CARS image produces low contrast (dark) around the center of beads, while the image produces high contrast (bright) at the peripheral part of the beads, which can be understood by considering the phase-matching condition [40]. Around the center of a bead, the CARS radiation builds up in the forward direction through the focal volume, due to the phase matching condition. This is because the bead diameter (10 mm) is sufficiently larger than the focal volume (~5 μm [33]). On the contrary, the CARS signal in the backward direction is efficiently suppressed by destructive interference, at the expense of constructive interference in the forward direction. Similar phenomena were observed in third harmonic generation (THG) imaging in the forward observation [50]. Intracellular lipid droplets (LDs) can be visualized by the THG signal. Small LDs give THG spots, while large LDs appear as rings.

Since the coherent buildup of the CARS radiation does not perfectly take place at the peripheral part of beads, the backward CARS signal is relatively more intense at the peripheral than at the center of beads. On the contrary, the situation is the opposite of the forward CARS image (Supplement 1, Fig. S1) which shows high contrast at the center of beads (inset in Supplement 1, Fig. S1).

3.2. Backward CARS imaging of EpH4 cells

To evaluate the applicability of this method to the life sciences, we demonstrated backward CARS imaging of EpH4 cells with the EM-gain mode. As for the cultured cell, the backward CARS signal is weak, and the forward CARS signal is hardly detected in the backward direction due to the thickness and transparency of the cells. Figure 5 represents the backward CARS image at 2850 cm^{-1} (CH_2 stretching mode due to lipids) and 2930 cm^{-1}(CH_3 stretching mode due to protein and lipids) with the exposure time of 100 ms/pixel, accompanied with bright-field image obtained after the measurement. We used laser powers with approximately 250 and 170 mW for ω_1 and ω_2. Intracellular small organelles on the order of a few micrometers were visualized with an exposure time of only 100 ms/pixel. [44,45], small structures in the orders of incident laser wavelength are mainly observed, because backscattered forward CARS signal is negligible for EpH4 cells, and inherent backward CARS signal is dominant. Particles of approximately 2 μm are observed in CARS images both at 2850 cm^{-1} and 2930 cm^{-1} in Fig. 5(a). In addition, structures of approximately 5 μm can be seen in the CARS image at 2930 cm^{-1} within the region enclosed by a white dashed line. Figure 5(b) shows the spectral profile of the imaginary part of $\chi^{(3)}$ ($\mathrm{Im}[\chi^{(3)}]$) at the organelles indicated by the arrows (i) and (ii). The $\mathrm{Im}[\chi^{(3)}]$) spectrum corresponds to vibrationally resonant spectrum, which is equivalent to the spontaneous Raman spectrum. The conversion from the CARS spectrum to the $\mathrm{Im}[\chi^{(3)}]$ is retrieved by using the maximum entropy method [51]. In Fig. 5(b), the spectral profile only in the CH region (2800 - 3000cm^{-1}) is shown because the Raman bands in the fingerprint region (600 - 1800cm^{-1}) were hardly observed due to fringing caused by etaloning of the EM-CCD camera. Although the fingerprint vibrational modes were not used in the present study, each spectrum is clearly different

OPTICS CONTINUUM

between (i) and (ii) even in the CH stretching region. The spectral profile of $\mathrm{Im}[\chi^{(3)}]$ indicated by (i) shows the vibrational signature of lipids at 2850 cm^{-1} due to CH_2 stretching vibrational mode. On the other hand, the spectral profile indicated by (ii) shows the vibrational signature of proteins at 2930 cm^{-1} due to CH_3 stretching vibrational mode [28], the small organelles indicated by (i) and (ii) are safely assigned as LDs and nucleoli, because the former is rich in lipids, while the latter is rich in protein.

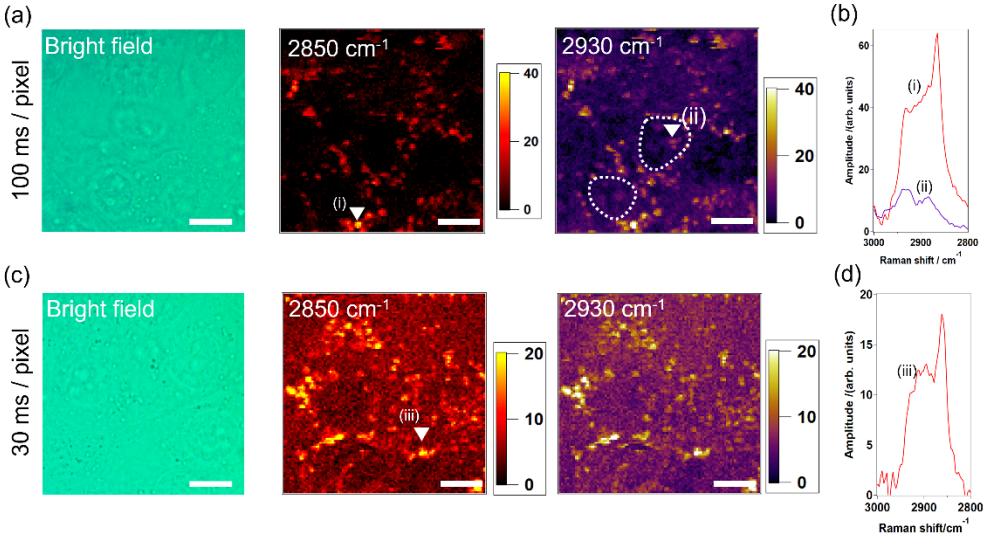

Fig. 5. Backward CARS image of EpH4 cells with an EM-CCD camera. (a) Bright field and backward CARS images at 2850 cm^{-1} and 2930 cm^{-1} with exposure time of 100 ms. (b) $\mathrm{Im}[\chi^{(3)}]$ spectrum indicated by the white arrows (i) and (ii) in (a). (c) Bright field and backward CARS images at 2850 cm^{-1} and 2930 cm^{-1} with exposure time of 30 ms. (d) $\mathrm{Im}[\chi^{(3)}]$ spectrum indicated by the white arrow (iii) in (c). The image size (pixels and microns) and step size were 101×101, 50×50 $\mu\mathrm{m}^2$, and 0.5 µm. Scale bar is 10 µm. The broken lines in (c) indicate the positions of nuclei.

These trends have been effectively extracted using multivariate curve resolution-alternating least squares (MCR-ALS) method [52,53]. By specifically focusing on the CH stretching region, we have successfully decomposed the spectra and images associated with lipids, proteins, and water both for the forward and backward CARS data as shown in Fig. S2. However, in contrast to the successful decomposition in the CH stretching region, our attempts at spatio-spectral decomposition in the fingerprint region using MCR-ALS were hindered by a significant etaloning effect. Consequently, we were unable to achieve the desired decomposition results in this region.

Next, we tried to see if we could capture CARS images at a higher speed than 100 ms/pixel. The results obtained by 30 ms/pixel are shown in Fig. 5(c). Although the SNR is worse than that with 100 ms/pixel, we have successfully observed LDs (indicated by the white arrows (iii)) even with short exposure times such as our previous study [28,29]. The results above demonstrate that micrometer-sized organelles within cells can be spectroscopically identified in just 100 ms/pixel using our method. This confirms that the method developed in the present study is suitable for live-cell imaging.

4. Conclusion

In this study, we developed a backward multiplex CARS spectroscopic imaging system with an EM-CCD camera. As a standard sample, we measured the CARS spectrum of polystyrene

OPTICS CONTINUUM

beads in the backward configuration and were able to obtain the CARS spectrum in the spectral range of 3500 cm^{-1}. Measuring the CARS signal using an EM-CCD camera improved SNR by approximately three times compared to that using a conventional CCD camera, validating the usefulness of an EM-CCD camera. The intra-cellular organelles such as LDs and nucleoli in cultured epithelial cells were visualized and spectroscopically identified in the backward CARS configuration even with the exposure time of 100 ms/pixel proving the powerfulness of the system as a spectroscopic imaging system. Therefore, we believe that these results justify further investigation into the combination of CARS and conventional inverted microscopes. This could potentially contribute to the development of more advanced imaging techniques including other multiphoton imaging methods. Our state-of-the-art imaging system will provide exceptional potential for real-time spectroscopic imaging of living cells, enabling revolutionary molecular diagnostics in both experimental and clinical applications.

Funding. Japan Society for the Promotion of Science (21H04961); JST-Mirai Program (JPMJMI22G5); Agence Nationale de la Recherche (ANR-10-LABX-0074 Sigma-LIM).

Acknowledgments. The authors would like to express their gratitude to J. Ukon of Ukon Craft Science, Ltd., for facilitating the collaboration between the Japanese and French laboratories. Additionally, the authors would like to extend their appreciation to Tokyo Instruments, Inc. for generously providing the EM-CCD camera used in this study. The authors would also like to thank Dr. Shinichi Miyazaki for his valuable assistance with the MCR-ALS analysis.

Disclosures. The authors declare that they have no conflict of interest.

Data availability. The datasets generated and/or analyzed during the current study are available from the corresponding author upon reasonable request.

Supplemental document. See Supplement 1 for supporting content.

References

1. T. C. Bakker Schut, R. Wolthuis, P. J. Caspers, and G. J. Puppels, "Real-time tissue characterization on the basis ofin vivo Raman spectra," J. Raman Spectrosc. **33**(7), 580–585 (2002).
2. C. L. Evans, E. O. Potma, M. Puoris'haag, D. Cote, C. P. Lin, and X. S. Xie, "Chemical imaging of tissue in vivo with video-rate coherent anti-Stokes Raman scattering microscopy," Proc. Natl. Acad. Sci. U. S. A. **102**(46), 16807–16812 (2005).
3. Z. Movasaghi, S. Rehman, and I. U. Rehman, "Raman Spectroscopy of Biological Tissues," Appl. Spectrosc. Rev. **42**(5), 493–541 (2007).
4. C. L. Evans and X. S. Xie, "Coherent Anti-Stokes Raman Scattering Microscopy: Chemical Imaging for Biology and Medicine," Annu. Rev. Anal. Chem. **1**(1), 883–909 (2008).
5. X. S. X. Ji-Xin Cheng, *Coherent Raman Scattering Microscopy*, CRC Press (2012).
6. J.-X. Cheng and X. S. Xie, "Vibrational spectroscopic imaging of living systems: An emerging platform for biology and medicine," Science **350**(6264), aaa8870 (2015).
7. M. Cicerone, "Molecular imaging with CARS micro-spectroscopy," Curr. Opin. Chem. Biol. **33**, 179–185 (2016).
8. D. Fu, "Quantitative chemical imaging with stimulated Raman scattering microscopy," Curr. Opin. Chem. Biol. **39**, 24–31 (2017).
9. D. Wang, P. He, Z. Wang, G. Li, N. Majed, and A. Z. Gu, "Advances in single cell Raman spectroscopy technologies for biological and environmental applications," Curr. Opin. Biotechnol. **64**, 218–229 (2020).
10. M. D. Duncan, J. Reintjes, and T. J. Manuccia, "Scanning coherent anti-Stokes Raman microscope," Opt. Lett. **7**(8), 350 (1982).
11. A. Zumbusch, G. R. Holtom, and X. S. Xie, "Three-dimensional vibrational imaging by coherent anti-Stokes Raman scattering," Phys. Rev. Lett. **82**(20), 4142–4145 (1999).
12. M. Hashimoto, T. Araki, and S. Kawata, "Molecular vibration imaging in the fingerprint region by use of coherent anti-Stokes Raman scattering microscopy with a collinear configuration," Opt. Lett. **25**(24), 1768–1770 (2000).
13. E. Ploetz, S. Laimgruber, S. Berner, W. Zinth, and P. Gilch, "Femtosecond stimulated Raman microscopy," Appl. Phys. B **87**(3), 389–393 (2007).
14. C. W. Freudiger, W. Min, B. G. Saar, S. Lu, G. R. Holtom, C. He, J. C. Tsai, J. X. Kang, and X. S. Xie, "Label-Free Biomedical Imaging with High Sensitivity by Stimulated Raman Scattering Microscopy," Science **322**(5909), 1857–1861 (2008).
15. Y. Ozeki, F. Dake, S. I. Kajiyama, K. Fukui, and K. Itoh, "Analysis and experimental assessment of the sensitivity of stimulated Raman scattering microscopy," Opt. Express **17**(5), 3651–3658 (2009).
16. V. V. Pully, A. Lenferink, and C. Otto, "Hybrid Rayleigh, Raman and two-photon excited fluorescence spectral confocal microscopy of living cells," J. Raman Spectrosc. **41**(6), 599–608 (2010).
17. C. Scalfi-Happ, M. Udart, C. Hauser, and A. Rück, "Investigation of lipid bodies in a colon carcinoma cell line by confocal Raman microscopy," Medical Laser Application **26**(4), 152–157 (2011).

OPTICS CONTINUUM

18. V. V. Pully, A. T. M. Lenferink, and C. Otto, "Time-lapse Raman imaging of single live lymphocytes," J. Raman Spectrosc. **42**(2), 167–173 (2011).
19. D. Fu, F.-K. Lu, X. Zhang, C. Freudiger, D. R. Pernik, G. Holtom, and X. S. Xie, "Quantitative Chemical Imaging with Multiplex Stimulated Raman Scattering Microscopy," J. Am. Chem. Soc. **134**(8), 3623–3626 (2012).
20. M. Li, Y. Ueyama-Toba, M. Lindley, G. Kongklad, Y. Nawa, Y. Kumamoto, S. Ishida, Y. Kanda, S. Fujita, H. Mizuguchi, and K. Fujita, "Label-Free Evaluation of Maturation and Hepatotoxicity of Human iPSC-Derived Hepatocytes Using Hyperspectral Raman Imaging," Anal. Chem. **95**(24), 9252–9262 (2023).
21. L. Wei, Z. Chen, L. Shi, R. Long, A. V. Anzalone, L. Zhang, F. Hu, R. Yuste, V. W. Cornish, and W. Min, "Super-multiplex vibrational imaging," Nature **544**(7651), 465–470 (2017).
22. T. W. Kee and M. T. Cicerone, "Simple approach to one-laser, broadband coherent anti-Stokes Raman scattering microscopy," Opt. Lett. **29**(23), 2701–2703 (2004).
23. H. Kano and H. Hamaguchi, "Ultrabroadband (> 2500 cm(-1)) multiplex coherent anti-Stokes Raman scattering microspectroscopy using a supercontinuum generated from a photonic crystal fiber," Appl. Phys. Lett. **86**(12), 1 (2005).
24. G. I. Petrov and V. V. Yakovlev, "Enhancing red-shifted white-light continuum generation in optical fibers for applications in nonlinear Raman microscopy," Opt. Express **13**(4), 1299–1306 (2005).
25. G. I. Petrov, R. Arora, V. V. Yakovlev, X. Wang, A. V. Sokolov, and M. O. Scully, "Comparison of coherent and spontaneous Raman microspectroscopies for noninvasive detection of single bacterial endospores," Proc. Natl. Acad. Sci. U. S. A. **104**(19), 7776–7779 (2007).
26. C. H. Camp Jr, Y. J. Lee, J. M. Heddleston, C. M. Hartshorn, A. R. H. Walker, J. N. Rich, J. D. Lathia, and M. T. Cicerone, "High-speed coherent Raman fingerprint imaging of biological tissues," Nat. Photonics **8**(8), 627–634 (2014).
27. C. H. Camp Jr and M. T. Cicerone, "Chemically sensitive bioimaging with coherent Raman scattering," Nat. Photonics **9**(5), 295–305 (2015).
28. H. Yoneyama, K. Sudo, P. Leproux, V. Couderc, A. Inoko, and H. Kano, "CARS molecular fingerprinting using sub-100-ps microchip laser source with fiber amplifier," APL Photonics **3**(9), 092408 (2018).
29. H. Kano, T. Maruyama, J. Kano, Y. Oka, D. Kaneta, T. Guerenne, P. Leproux, V. Couderc, and M. Noguchi, "Ultra-multiplex CARS spectroscopic imaging with 1-millisecond pixel dwell time," OSA Continuum **2**(5), 1693–1705 (2019).
30. A. C. Murthy, G. L. Dignon, Y. Kan, G. H. Zerze, S. H. Parekh, J. Mittal, and N. L. Fawzi, "Molecular interactions underlying liquid–liquid phase separation of the FUS low-complexity domain," Nat. Struct. Mol. Biol. **26**(7), 637–648 (2019).
31. K. Ishitsuka, M. Koide, M. Yoshida, H. Segawa, P. Leproux, V. Couderc, M. M. Watanabe, and H. Kano, "Identification of intracellular squalene in living algae,Aurantiochytrium mangroveiwith hyper-spectral coherent anti-Stokes Raman microscopy using a sub-nanosecond supercontinuum laser source," J. Raman Spectrosc. **48**(1), 8–15 (2017).
32. Y. Oka, M. Yoshida, A. Minoda, P. Leproux, M. M. Watanabe, and H. Kano, "Label-free detection of polysulfides and glycogen of Cyanidium caldarium using ultra-multiplex coherent anti-Stokes Raman scattering microspectroscopy," J. Raman Spectrosc. **52**(12), 2572–2580 (2021).
33. K. Tanaka, R. Oketani, T. Terada, P. Leproux, Y. Morono, and H. Kano, "Label-Free Identification of Spore-Forming Bacteria Using Ultrabroadband Multiplex Coherent Anti-Stokes Raman Scattering Microspectroscopy," J. Phys. Chem. B **127**(9), 1940–1946 (2023).
34. F. Vernuccio, R. Vanna, C. Ceconello, A. Bresci, F. Manetti, S. Sorrentino, S. Ghislanzoni, F. Lambertucci, O. Motiño, I. Martins, G. Kroemer, I. Bongarzone, G. Cerullo, and D. Polli, "Full-Spectrum CARS Microscopy of Cells and Tissues with Ultrashort White-Light Continuum Pulses," J. Phys. Chem. B **127**(21), 4733–4745 (2023).
35. R. Imai and H. Kano, "Label-free enzymatic reaction monitoring in water-in-oil microdroplets using ultra-broadband multiplex coherent anti-Stokes Raman scattering spectroscopy," Biomed. Opt. Express **13**(3), 1506–1515 (2022).
36. R. Poorna, W.-W. Chen, P. Qiu, and M. T. Cicerone, "Toward Gene-Correlated Spatially Resolved Metabolomics with Fingerprint Coherent Raman Imaging," J. Phys. Chem. B **127**(25), 5576–5587 (2023).
37. L. Gong, W. Zheng, Y. Ma, and Z. Huang, "Higher-order coherent anti-Stokes Raman scattering microscopy realizes label-free super-resolution vibrational imaging," Nat. Photonics **14**(2), 115–122 (2020).
38. C. Zong, R. Cheng, F. Chen, P. Lin, M. Zhang, Z. Chen, C. Li, C. Yang, and J.-X. Cheng, "Wide-Field Surface-Enhanced Coherent Anti-Stokes Raman Scattering Microscopy," ACS Photonics **9**(3), 1042–1049 (2022).
39. W. Peterson, K. Hiramatsu, and K. Goda, "The marriage of coherent Raman scattering imaging and advanced computational tools," Light: Sci. Appl. **12**(1), 113 (2023).
40. J. X. Cheng, A. Volkmer, and X. S. Xie, "Theoretical and experimental characterization of coherent anti-Stokes Raman scattering microscopy," J. Opt. Soc. Am. B **19**(6), 1363–1375 (2002).
41. E. Capitaine, N. O. Moussa, C. Louot, S. M. Bardet, H. Kano, L. Duponchel, P. Lévêque, V. Couderc, and P. Leproux, "Fast epi-detected broadband multiplex CARS and SHG imaging of mouse skull cells," Biomed. Opt. Express **9**(1), 245–253 (2018).
42. A. Lombardini, V. Mytskaniuk, S. Sivankutty, E. R. Andresen, X. Chen, J. Wenger, M. Fabert, N. Joly, F. Louradour, A. Kudlinski, and H. Rigneault, "High-resolution multimodal flexible coherent Raman endoscope," Light: Sci. Appl. **7**(1), 10 (2018).

OPTICS CONTINUUM

43. E. Pshenay-Severin, H. Bae, K. Reichwald, G. Matz, J. Bierlich, J. Kobelke, A. Lorenz, A. Schwuchow, T. Meyer-Zedler, M. Schmitt, B. Messerschmidt, and J. Popp, "Multimodal nonlinear endomicroscopic imaging probe using a double-core double-clad fiber and focus-combining micro-optical concept," Light: Sci. Appl. **10**(1), 207 (2021).
44. J. X. Cheng, A. Volkmer, L. D. Book, and X. S. Xie, "An epi-detected coherent anti-stokes raman scattering (E-CARS) microscope with high spectral resolution and high sensitivity," J. Phys. Chem. B **105**(7), 1277–1280 (2001).
45. A. Volkmer, J. X. Cheng, and X. S. Xie, "Vibrational imaging with high sensitivity via epidetected coherent anti-Stokes Raman scattering microscopy," Phys. Rev. Lett. **87**(2), 023901 (2001).
46. M. C. Weikl, F. Beyrau, J. Kiefer, T. Seeger, and A. Leipertz, "Combined coherent anti-Stokes Raman spectroscopy and linear Raman spectroscopy for simultaneous temperature and multiple species measurements," Opt. Lett. **31**(12), 1908–1910 (2006).
47. K. Hamada, K. Fujita, N. I. Smith, M. Kobayashi, Y. Inouye, and S. Kawata, "Raman microscopy for dynamic molecular imaging of living cells," J. Biomed. Opt. **13**(04), 1 (2008).
48. S. Kizawa and M. Hashimoto, "Ultrahigh-speed multiplex coherent anti-Stokes Raman scattering microspectroscopy using scanning elliptical focal spot," J Chem. Phys. **155**(14), 144201 (2021).
49. Y. Takei, R. Hirai, A. Fukuda, S. Miyazaki, R. Shimada, Y. Okamatsu-Ogura, M. Saito, P. Leproux, K. Hisatake, and H. Kano, "Visualization of intracellular lipid metabolism in brown adipocytes by time-lapse ultra-multiplex CARS microspectroscopy with an onstage incubator," J Chem. Phys. **155**(12), 125102 (2021).
50. D. Débarre, W. Supatto, A.-M. Pena, A. Fabre, T. Tordjmann, L. Combettes, M.-C. Schanne-Klein, and E. Beaurepaire, "Imaging lipid bodies in cells and tissues using third-harmonic generation microscopy," Nat. Methods **3**(1), 47–53 (2006).
51. E. M. Vartiainen, H. A. Rinia, M. Müller, and M. Bonn, "Direct extraction of Raman line-shapes from congested CARS spectra," Opt. Express **14**(8), 3622–3630 (2006).
52. M. Ando and H. Hamaguchi, "Molecular component distribution imaging of living cells by multivariate curve resolution analysis of space-resolved Raman spectra," J. Biomed. Opt. **19**(1), 011016 (2013).
53. D. Boildieu, T. Guerenne-Del Ben, L. Duponchel, V. Sol, J.-M. Petit, É. Champion, H. Kano, D. Helbert, A. Magnaudeix, P. Leproux, and P. Carré, "Coherent anti-Stokes Raman scattering cell imaging and segmentation with unsupervised data analysis," Front. Cell Dev. Biol. **10**, 1 (2022).